Programmable plasmonic phase modulation of free-space wavefronts at gigahertz rates

Alexei Smolyaninov [®]*, Abdelkrim El Amili, Felipe Vallini, Steve Pappert and Yeshaiahu Fainman

Space-variant control of optical wavefronts is important for many applications in photonics, such as the generation of structured light beams, and is achieved with spatial light modulators. Commercial devices, at present, are based on liquid-crystal and digital micromirror technologies and are typically limited to kilohertz switching speeds. To realize significantly higher operating speeds, new technologies and approaches are necessary. Here we demonstrate two-dimensional control of free-space optical fields at a wavelength of 1,550 nm at a 1 GHz modulation speed using a programmable plasmonic phase modulator based on near-field interactions between surface plasmons and materials with an electrooptic response. High $\chi^{(2)}$ and $\chi^{(3)}$ dielectric thin films of either aluminium nitride or silicon-rich silicon nitride are used as an active modulation layer in a surface plasmon resonance configuration to realize programmable space-variant control of optical wavefronts in a 4×4 pixel array at high speed.

patial light modulators (SLMs) are a class of devices that impose a space-variant amplitude and/or phase modulation on a light beam propagating in free space. In effect, SLMs can be thought of as a two-dimensional array of individually addressed free-space optical modulators. Phase-shifting SLMs enable numerous applications in various fields, including displays, biomedical in vivo imaging through scattering media, compact beam steering for LiDAR (light detection and ranging), wavefront encoding for holographic data storage and fast programmable optical tweezers.

Commercial SLM technologies using a variety of electrooptic transducers, including digital micromirror devices and ferroelectric liquid crystals have reported operating speeds up to $10\,\mathrm{kHz}$ (ref. 3). State-of-the-art research systems (Supplementary Section 3) using interferometric microelectromechanical system (MEMS) tuned subwavelength grating resonators have demonstrated modulation speeds as high as $500\,\mathrm{kHz}$ (ref. 4) with pixel pitches ranging from $10\,\mu\mathrm{m}$ to $120\,\mu\mathrm{m}$ (refs. $^{2-4}$). Recently, there has been a concerted effort to increase the operating speed of electronically driven SLMs5.6 to enable novel applications such as real-time, high-spatial-resolution, three-dimensional LiDAR sampling and holographic video 8.

There are two characteristics that limit the potential modulation bandwidth of an SLM: the speed of the electrooptic transducer material and the response time of the electronics addressing the transducer. So far, SLMs have been limited primarily by the speed of the transducer material, but not by the high-speed driving electronics. Current optical modulation technology operates at gigahertz bandwidths9. For example, guided wave integrated plasmonic modulators have demonstrated amplitude and phase modulation at speeds exceeding 100 GHz utilizing a combination of plasmonic localization and the linear electrooptic (Pockel's) effect¹⁰. Such devices typically consist of integrated photonic waveguides coupled to a plasmonic waveguide in a Mach-Zehnder interferometer (MZI) configuration embedded in an organic polymer with a high second-order nonlinear susceptibility, $\chi^{(2)}$ (refs. 9,10). This approach, combining the surface plasmon interaction with the linear electrooptic effect, can be extended to free-space systems.

A surface plasmon polariton is a charge density oscillation propagating at the interface between a metal and a dielectric 11-13.

In the Kretschmann configuration^{14–25}, a transverse magnetic polarized wave coming from a high-index prism is incident on a thin metal film, beyond which is a lower-index sensing layer. When the longitudinal component of the photonic wavevector k_x is matched to the surface plasmon wavevector $k_{\rm sp}$, a sharp resonance in both the reflected phase and amplitude as a function of incident angle and wavelength is observed. This surface plasmon resonance (SPR) is extremely sensitive to small changes in the refractive index (Δn) at both metal-dielectric interfaces11 and has been used for biomedical sensing¹⁴. A space-multiplexed variation of this technique, surface plasmon resonance imaging (SPRI), utilizes a charge-coupled device (CCD) detector to image the SPR signal from a two-dimensional array of thin-metal patch transducers simultaneously^{15–20}. Moreover, phase-sensitive SPRI extends this parallelism to interferometric and polarimetric configurations to achieve higher sensitivity in multiplexed SPR systems¹⁸⁻²². The extreme sensitivity of SPR to perturbations in the refractive index has likewise seen numerous applications in thin-film metrology²³. However, the refractive index of the sensing layer need not be fixed; it can be tuned slowly via thermal effects or, as we propose in this manuscript, quickly via the electrooptic effect. Indeed, SPR-based SLMs have been realized using a liquid-crystal active layer in the Kretschmann configuration, but they share the same speed limitations as commercial liquid-crystal SLMs^{24,25}. To realize truly high-speed space-variant light modulation, one needs to develop a high-speed electrooptic transducing mechanism.

In this Article we use a high $\chi^{(2)}$ dielectric thin film as the active layer in a programmable plasmonic phase modulator (PPPM) array based on the SPRI Kretschmann configuration to achieve phase-dominant, space-variant light modulation of free-space optical modes. The PPPM exploits the linear and quadratic electrooptic effects to achieve fast, space-variant refractive index modulation of a thin-film active layer. Using this approach, we realize phase-dominant 4×4 spatial light modulation with individual pixel modulation speeds of 1 GHz. Gigahertz modulation is evaluated by placing the PPPM in a free-space MZI and measuring the optical extinction ratios. A proof-of-concept demonstration of space-variant light modulation is performed via polarization contrast imaging to spell out the letters of 'UCSD'.

ARTICLES NATURE PHOTONICS

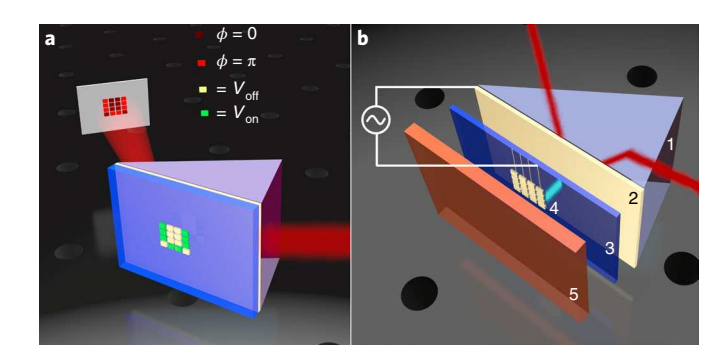


Fig. 1 | PPPM overview. a, Illustration of PPPM operation. b, Expanded view of the PPPM: (1) Si prism; (2) noble metal thin film for SPR (48 nm Ag); (3) electrooptic dielectric modulation layer of SRN or AIN; (4) 4×4 electrode matrix used to apply a field to the modulation layer; (5) sapphire wafer, which hosts the electrode matrix and electrooptic thin film. The patterned sapphire wafer is mechanically clamped to the Si prism, thereby achieving optical contact between the modulation layer and SPR metal layer of Ag. This forms a 4 × 4 array of parallel plate capacitors between the electrode matrix, dielectric thin film and SPR metal layer. A voltage is applied to one or more of the lead wires while the SPR thin metal film is kept grounded. This results in an electric field dropping across the modulation layer, which causes a shift in the local refractive index. The optical beam is incident at an almost normal angle to the input interface, totally internally reflected off the output face of the Si prism, incident on the Ag metal thin film at surface plasmon angle θ_{sp} and then reflected out. More detailed schematics of all the interfaces are available in Supplementary Section 1.

Results

The PPPM, illustrated in Fig. 1, consists of two components. The first is a Brewster angle silicon prism with a 48 nm silver thin film deposited via radiofrequency (RF) sputtering. A silicon prism is selected to satisfy the phase-matching condition where the refractive index of the prism must be greater than the refractive index of the active layer (Supplementary Section 1). The second is a sapphire wafer with a 4×4 matrix of $45 \,\mu\text{m} \times 30 \,\mu\text{m}$ gold electrodes and 8-µm-wide lead wires, above which an active layer consisting of an inorganic high $\chi^{(2)}$ and $\chi^{(3)}$ dielectric thin film is deposited. For the dielectric layer, both RF-sputtered aluminium nitride (AlN) and plasma-enhanced chemical vapour deposition (PECVD)-deposited silicon-rich silicon nitride (SRN) of varying thicknesses were investigated. The dielectric film fully covers the 4×4 matrix of gold electrodes but does not cover the lead wires near the top of the wafer, allowing for electric contact with the electrode matrix (Fig. 1b). Optical contact is achieved by mechanically clamping the patterned sapphire wafer to the Si prism, in effect forming a 4×4 array of parallel plate capacitors between the electrode matrix, dielectric thin film and SPR metal layer. Further illustrations of the device as well as the optical path within the assembled PPPM are provided in Supplementary Section 1. A voltage is applied to one or more of the lead wires and the SPR thin film is kept grounded. The individual gold electrodes of the electrode matrix over the SPR thin film act as a parallel plate capacitor. A quasi-uniform electric field is created between the electrodes and the SPR layer, thereby inducing a refractive index variation Δn in the $\chi^{(2)}$ dielectric beneath a particular electrode. When considering Pockel's effect, of principal interest to us is the Δn induced due to the r_{33} component of the refractive index ellipsoid oriented along the direction of the applied electric field and normal to the SPR thin metal film. We can therefore reduce the full refractive index ellipsoid to a scalar value, where r_{33} is related to the second-order electric susceptibility $\chi^{(2)}$ by $r_{33} = \frac{2\chi^{(2)}}{\epsilon^2}$. Here, E is the electric field applied across the dielectric, and ϵ_r is the relative permittivity of the dielectric.

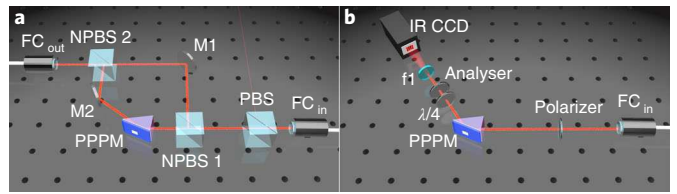


Fig. 2 | Experimental set-up. a, MZI experimental set-up for quantifying single-pixel performance. $FC_{in'}$ input fibre coupler; PBS, polarizing beamsplitter; NPBS, non-polarizing beamsplitter (1,550 nm); M, mirror; $FC_{out'}$ output fibre coupler. **b**, SPR polarization contrast imaging set-up. Light is polarized at $P+45^{\circ}$. The light is incident on the described PPPM where SPR adds a further phase delay between P and S components of the light. The light then passes through a quarterwave plate and an analyser at $P-32.1^{\circ}$. The resulting intensity profile is expanded using a lens doublet (f1) and projected onto an FLIR sc2600 CCD camera. More detailed schematics are provided in Supplementary Section 2.

For this Article we consider Δn to be the result of the second-order nonlinearity $\chi^{(2)}$ in AlN $(r_{33} \approx 1.0 \,\mathrm{pm}\,\mathrm{V}^{-1})^{27}$ or SRN $(r_{33} \approx 0.1 \text{ pm V}^{-1})$. While there is good agreement in the literature as to the values of $\chi^{(2)}$ and r_{33} for AlN at 1,550 nm, at the time of writing the magnitude and precise mechanism of the effective $\chi^{(2)}$ as well as $\chi^{(3)}$ contributions in SRN were still a topic of active research²⁸. This electrically induced Δn creates a phase shift after reflection due to coupling into the SPR modes at the metal-dielectric interface. The phase shift in a reflected beam due to SPR can be calculated analytically from the Fresnel equations^{29–31} (Supplementary Section 1). Critically, when biased at the correct angle of incidence, high-purity phase modulation of incident p-polarized light can be achieved using this method (Supplementary Section 1). Conversely, incident s-polarized light undergoes no SPR-induced phase shift. This discrepancy forms the basis of SPR-based polarimetry, ellipsometry and phase-contrast imaging14,19,20,32

Dynamic characterization at 1 GHz. To investigate the dynamic behaviour of our device, we characterized the high-frequency electrooptic modulation of the PPPM using a free-space MZI, as illustrated in Fig. 2a. Space-variant light modulation was then demonstrated under d.c. conditions using a well-established polarization contrast imaging technique based on SPR ellipsometry. For all measurements, a 48 nm Ag film deposited on the Si prism via electron-beam evaporation was used as the SPR layer, while the excitation wavelength was 1,550 nm.

Interferometric measurements using the set-up of Fig. 2a produce fringes. Conceptually, applying a phase shift to one arm of the interferometer with respect to the other shifts these fringes. If the aperture of the light-collecting optics at the output of the interferometer is less than half the period of these fringes, then the measured optical signal will vary with the induced phase shift as the fringes are shifted across the collecting optic. In this manner, interference in the MZI translates the induced phase modulation of the PPPM into an amplitude modulation at the MZI output. For the MZI measurement, a fibre-coupled 1,550 nm source is p-polarized, collimated and split along a modulated arm and a reference arm using a 90-10 non-polarizing beamsplitter (NPBS). A consequence of using SPR is a relatively high insertion loss, so the MZI achieves a coarse balancing by sending 90% of the light to the modulator arm. In the modulated arm, a single pixel of the electrode matrix is fed with a sinusoidal waveform from an electrical synthesizer at a frequency of 1 GHz with an RF power of 21 dBm. The driving field drops off across the nonlinear dielectric between the electrode and the 48 nm Ag film. Light from the two arms is recombined using a 50-50 NPBS and then fibre coupled NATURE PHOTONICS ARTICLES

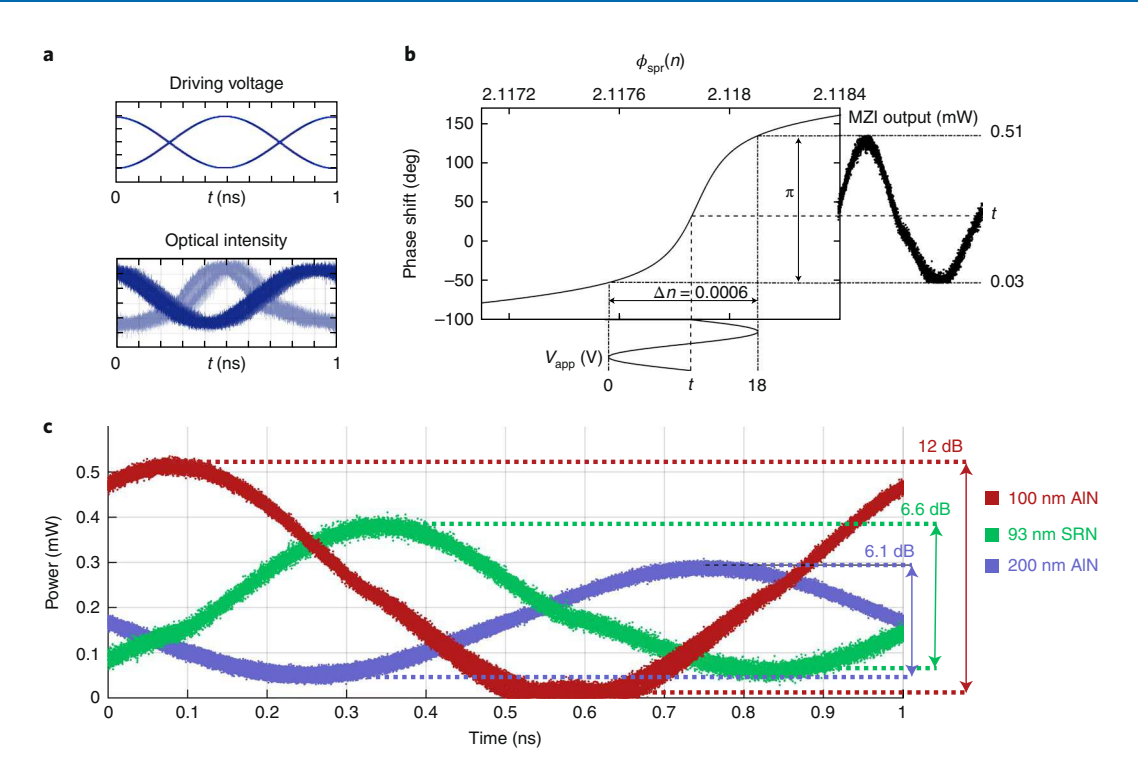


Fig. 3 | Dynamic characterization. a, Temporal characteristics of the electronic driving signal from the synthesizer and measured optical intensity of the MZI using an AIN matrix. Two 1 ns samples of each signal are presented with a -3π phase offset **b**, Theoretical phase shift ϕ_{spr} as a function of Δn for 48 nm Ag thin film on a silicon prism and 100 nm of AIN with 18 V peak-to-peak modulated applied voltage overlay. Inset curves showing applied voltage and measured MZI intensity output as a function of time illustrate the electrooptic transfer mechanism of the PPPM. An applied potential of 18 V shifts the refractive index by 0.0006 refractive index units in the modulation layer, producing a relative π phase shift in the reflected beam that modulates the intensity of the MZI with an extinction ratio of 12 dB. **c**, Measured optical intensity in mW at the output of the MZI using three different active layer materials. Red: 100-nm-thick AIN film with an 18 V sinusoidal driving signal, σ = 25 μW. Green: 93 nm SRN film at 25 V, σ = 23 μW. Blue: 200 nm AIN film at 18 V, σ = 21 μW. Extinction ratios are indicated on the right.

out and fed to an electrooptic converter. For additional details, see Methods

The gigahertz modulated optical signals of modulators with three different electrooptic thin films (100 nm film of AlN, 200 nm AlN film and 93 nm film of SRN) were evaluated. The most obvious effect of film thickness on the modulator is the applied field strength, which scales inversely with film thickness d. AlN films with d=100 nm and d=200 nm were modulated with a 1 GHz, 18 V peak-to-peak signal. This voltage was necessary to achieve a $\sim \pi$ phase shift in the AlN matrix and exceeds the calculated $V\pi$ (Supplementary Section 1) by 4 V; this was most probably caused by an air gap between the electrode matrix and the SPR thin film that occurred when making optical contact. SRN, which can tolerate significantly higher field strength relative to AlN³³ before reaching breakdown³⁴⁴,3⁵ (Supplementary Section 1), was modulated with a 1 GHz, 25 V signal for an SRN film thickness of 93 nm. See Methods and Supplementary Information for RF bandwidth.

Figure 3a presents the electronic sinusoidal driving signal at 1 GHz from the electronic synthesizer and the corresponding, quasi-sinusoidal measured time-variant optical intensity taken at the output of the MZI. The presented curves are for two 1 ns samples of both signals taken at a ~3 π phase offset (1.5 periods). Figure 3b illustrates the theoretical phase shift $\phi_{\rm spr}$ as a function of refractive index calculated from the Fresnel equations for a Si prismAg film-AlN system (Supplementary Section 1). Applied voltage and corresponding optical intensity curves from the 100 nm AlN sample are appended to the $\phi_{\rm spr}$ curve to illustrate the electrooptic transfer mechanism. As the applied voltage modulates the refractive index by Δn = 0.0006, $\phi_{\rm spr}$ undergoes a π phase shift, which

translates to an intensity modulation in the MZI of 12 dB. Figure 3c presents the modulated optical power at the output of the MZI as a function of time with a 1 GHz sinusoid as the driving signal. Extinction ratios of up to 12 dB were achieved in the case of the 100 nm AlN film. Unlike the driving signal (Fig. 3a), the observed intensity signals were not homogeneously symmetric sinusoids. There are several possible explanations for this behaviour. First, the electrooptic transfer of the modulator was not biased fully in the linear regime, that is, $\phi_{ ext{spr}}$ did not vary linearly with respect to the modulated refractive index (Fig. 3c). Second, surface roughness in the electrooptic film as well as the process of making optical contact between the sapphire wafer hosting the electrode matrix and the electrooptic thin film with the Si prism may lead to air gaps between the electrode matrix and prism, which would affect the applied field strength as well as the magnitude of the SPR shift. Other possible explanations for this quasi-sinusoidal behaviour include amplitude modulation due to angular offset from the optimal angular bias point (Supplementary Fig. 2) and a possible third-order nonlinear $\chi^{(3)}$ contribution to the observed electrooptic modulation.

Space-variant modulation. Having demonstrated phase-dominant electrooptic modulation for a single pixel of the PPPM at 1 GHz, we next demonstrate the feasibility of space-variant modulation using polarization contrast imaging. The imaging set-up was based on reported SPR polarization contrast imaging configurations in the literature, which are based on ellipsometric SPR measurements (Supplementary Section 2). A detailed theory of polarimetry and ellipsometry under SPR conditions can be found in numerous references^{14,21,32}, and the polarization contrast imaging configuration

ARTICLES NATURE PHOTONICS

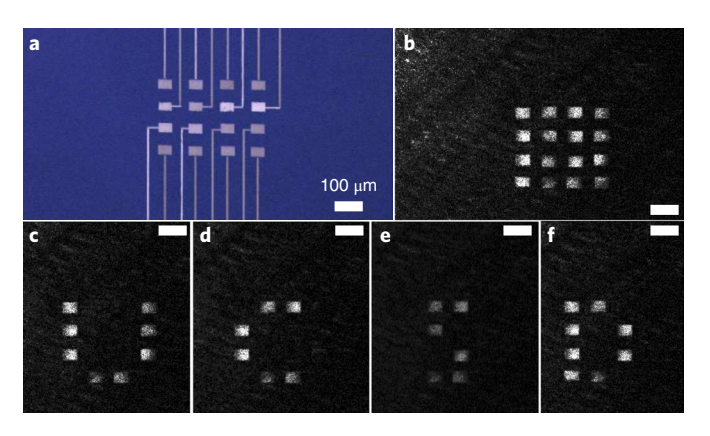


Fig. 4 | Space-variant modulation. a, Microscope image of the 4×4 PPPM, imaged through 100 nm AIN. Electrodes consist of 50 nm of Au on a sapphire substrate. **b**, Polarization contrast image taken at 1,550 nm using an FLIR SC2600 with a d.c. potential of 18 V applied to all pixels. Scale bar, 100 μm. **c**, Polarization contrast image with 18 V applied to only eight electrodes in the shape of a 'U'. **d**, Voltage applied to six electrodes in the shape of a 'C'. **e**, Voltage applied to six electrodes in the shape of an 'S'. **f**, Voltage applied to eight electrodes in the shape of a 'D'.

used here is directly based on refs. ^{17–20}. Briefly, incident light with some known polarization is incident on the Kretschmann configuration and undergoes SPR excitation and reflection (Fig. 2b). The phase and amplitude of the p-polarized component of light undergoes dramatic changes while the s-polarized component of light is unaltered. The light then passes through an analyser and the optical intensity is measured as a function of analyser angle. Phase retarding plates may be used to further adjust delay between p and s polarizations.

The individual pixels of the PPPM are depicted in Fig. 4a. Figure 4b-f shows the polarization contrast image of the output of the PPPM with varying inputs using the set-up illustrated in Fig. 2b. Figure 4b shows all of the pixels in the 'on' state with 18 V applied to each. Figure 4c-f shows pixels modulated to spell out the letters of 'UCSD'. Some visible non-uniformity can be attributed to surface roughness and minor impedance mismatches in the microstrip lines feeding the individual electrodes of the PPPM.

Discussion

The primary limitations of the presented PPPM as a high-speed, space-variant light modulator are insertion loss, drive voltage, stringent alignment angle, inter-pixel distance and phase modulation depth. The devices presented here serve as a demonstration experiment. We used readily available PECVD-deposited SRN and RF-sputtered AlN, which have relatively low r_{33} values of few pm V⁻¹. To compensate for this low effective r_{33} , the thickness of the SPR thin film was optimized to support a plasmon resonance in which the induced phase shift was maximized at the cost of increased insertion loss, and the PPPM was biased at an operating point with a narrow angular acceptance as discussed in Supplementary Section 1. Supplementary Fig. 2 indicates a theoretical insertion loss of 10 dB for the reported PPPM with a phase modulation of up to 1.1π . The reported π phase shift is sufficient to realize two-level binary phase control of light at gigahertz rates, which has potential applications such as discrete step beam steering^{36–38}.

These metrics are by no means a fundamental limitation of the reported phase modulation scheme, but rather a limitation of the electrooptic coefficient of the specific materials we used in this first demonstration. An avenue to overcome this limitation is to use higher r_{33} dielectric thin films such as recent advances in SRN thin films with electric-field-induced second harmonic generation²⁸,

the applications of which are discussed in the Supplementary Information. Additionally, much work has been done recently with lithium niobate on silicon, which has an even greater $I_{33} > 30 \text{ pm V}^{-1}$ (refs. ^{39,40}). Indeed, a PPPM with a 22 pm V⁻¹ active layer could have a predicted modulation depth of 2π , angular acceptance of 0.3° and theoretical insertion loss of <5 dB (Supplementary Figs. 2d, 10 and 11). Inter-pixel distance, an important figure of merit for SLMs that constrains the fill factor and therefore efficiency, is limited in the PPPM by the decay length of the excited surface plasmon (SP) as plasmonic crosstalk between adjacent pixels would be detrimental to device performance. Reduction in the inter-pixel distance may be accomplished by reducing the decay length of the excited plasmon; this may be achieved by introducing a material with a higher dielectric loss coefficient near the SP interface (Supplementary Section 4) or by patterning the plasmonic thin film with a periodic structure to more precisely control the excited SP wavevector¹¹.

When compared with the electrooptic transduction mechanisms used in state-of-the-art SLM schemes, such as MEMS, liquid crystal and thermooptic modulation, the electrooptic modulation of SPR in the Kretschmann configuration presented here realizes operating speeds over three orders of magnitude greater than the state of the art (Supplementary Section 3). The solid-state nature of our device provides additional advantages over state-of-the-art liquid crystal and MEMS-based approaches: solid-state devices have no moving parts and therefore offer innately superior mechanical stability when compared to MEMS, and they have significantly greater thermal stability when compared to organic liquid-crystal devices. The PPPM presented here was kept to a small 4×4 matrix to simplify the addressing electronics; this size is not indicative of a limiting case. In terms of electronics, integrated silicon photonic phased arrays with >300 elements have been demonstrated with pitches below 10 µm using through-silicon vias for high-density integration⁴¹; this greatly exceeds our density requirements and these same vias could be used to address the electrodes of an SPR-based SLM based on the transducing mechanism demonstrated in the PPPM. Finally, it is probably possible to miniaturize the PPPM reported in this work to a planar topology by transitioning to grating coupled SPR¹¹ rather than prism coupling.

Conclusions

In the presented work a 1 GHz programmable plasmonic phase modulator was used to realize space-variant phase control of incident light at a wavelength of 1,550 nm using electrooptic modulation of SPR in the Kretschmann configuration as the electrooptic transduction mechanism. High-speed MZI characterization of the PPPM at 1 GHz realized extinction ratios of 12 dB corresponding to a phase shift of $\sim \pi$. The reported phase shift is sufficient for twolevel binary phase control of light, with potential applications such as discrete step beam steering. More sophisticated applications, such as continuous beam steering, would require a full 2π phase shift; this may be achievable in the near term with the reported PPPM scheme using state-of-the-art material platforms with higher nonlinear coefficients such as lithium niobate on silicon. This realization of programmable space-variant light modulation at rates orders of magnitude beyond the kilohertz regime that is the current state of the art potentially offers a path toward true ultrahigh-speed spatial light modulation.

Online content

Any methods, additional references, Nature Research reporting summaries, source data, statements of data availability and associated accession codes are available at https://doi.org/10.1038/s41566-019-0360-3.

Received: 14 May 2018; Accepted: 8 January 2019;

Published online: 11 February 2019

NATURE PHOTONICS ARTICLES

References

- Dudley, D., Duncan, W. M. & Slaughter, J. Emerging digital micromirror device (DMD) applications. *Proc. SPIE* 4985, 14–26 (2003).
- Henderson, C. J., Leyva, D. G. & Wilkinson, T. D. Free space adaptive optical interconnect at 1.25 Gb/s, with beam steering using a ferroelectric liquidcrystal SLM. J. Lightwave Technol. 24, 1989–1997 (2006).
- Shrauger, V. & Warde, C. Development of a high-speed high-fillfactor phase-only spatial light modulator. Proc. SPIE 4291, 101–108 (2001).
- Yang, W. et al. High speed optical phased array using high contrast grating all-pass filters. Opt. Express 22, 20038–20044 (2014).
- Sun, T. et al. Surface-normal electro-optic spatial light modulator using graphene integrated on a high-contrast grating resonator. Opt. Express 24, 26035–26043 (2016).
- Yu, N. System, method and computer-accessible medium for depth of field imaging for three-dimensional sensing utilizing a spatial light modulator microscope arrangement. US patent application 14/763,925 (2015).
- Ahearn, J. S. et al. Multiple quantum well (MQW) spatial light modulators (SLMs) for optical data processing and beam steering. *Proc. SPIE* 4457, 43–54 (2001).
- Lucente, M., 2011. The first 20 years of holographic video—and the next 20. In Proc. 2nd Annual International Conference on Stereoscopic 3D for Media and Entertainment 21–23 (SMPTE, 2011).
- Haffner, C. et al. All-plasmonic Mach–Zehnder modulator enabling optical high-speed communication at the microscale. *Nat. Photon.* 9, 525–528 (2015).
- Hössbacher, C. et al. Plasmonic modulator with >170 GHz bandwidth demonstrated at 100 GBd NRZ. Opt. Express 25, 1762–1768 (2017).
- Zayats, A. V., Smolyaninov, I. I. & Maradudin, A. A. Nano-optics of surface plasmon polaritons. *Phys. Rep.* 408, 131–314 (2005).
- Tetz, K., Rokitski, R., Nezhad, M. & Fainman, Y. Excitation and direct imaging of surface plasmon polariton modes in a two-dimensional grating. *Appl. Phys. Lett* 86, 111110 (2005).
- Rokitski, R., Tetz, K. A. & Fainman, Y. Propagation of femtosecond surface plasmon polariton pulses on the surface of a nanostructured metallic film: space-time complex amplitude characterization. *Phys. Rev. Lett.* 95, 177401 (2005).
- Huang, Y. H., Ho, H. P., Wu, S. Y. & Kong, S. K. Detecting phase shifts in surface plasmon resonance: a review. Adv. Opt. Technol. 2012, 471957 (2012).
- Nakkach, M., Duval, A., Ea-Kim, B., Moreau, J. & Canva, M. Angulo-spectral surface plasmon resonance imaging of nanofabricated grating surfaces. Opt. Lett. 35, 2209–2211 (2010).
- Nikitin, P. I. et al. Surface plasmon resonance interferometry for micro-array biosensing. Sens. Actuat. A 85, 189–193 (2000).
- Dong, W. et al. Improved polarization contrast method for surface plasmon resonance imaging sensors by inert background gold film extinction. Opt. Commun. 346, 1–9 (2015).
- Piliarik, M., Vaisocherová, H. & Homola, J. A new surface plasmon resonance sensor for high-throughput screening applications. *Biosens. Bioelectron.* 20, 2104–2110 (2005).
- Piliarik, M., Katainen, J. & Homola, J. Novel polarization control for high-throughput surface plasmon resonance sensors. *Opt. Sens. Technol. Appl.* 6585, 658515 (2007).
- Homola, J. & Yee, S. S. Novel polarization control scheme for spectral surface plasmon resonance sensors. Sens. Actuat. B 51, 331–339 (1998).
- Huang, Y. H., Ho, H. P., Kong, S. K. & Kabashin, A. V. Phase-sensitive surface plasmon resonance biosensors: methodology, instrumentation and applications. *Ann. Phys.* 524, 637–662 (2012).
- Moirangthem, R. S., Chang, Y. C., Hsu, S. H. & Wei, P. K. Surface plasmon resonance ellipsometry based sensor for studying biomolecular interaction. *Biosens. Bioelectron.* 25, 2633–2638 (2010).
- 23. Liu, C., Liu, Q. & Hu, X. SPR phase detection for measuring the thickness of thin metal films. Opt. Express 22, 7574–7580 (2014).
- Yeatman, E. M. & Caldwell, M. E. Spatial light modulation using surface plasmon resonance. Appl. Phys. Lett. 55, 613–615 (1989).
- Kogan, P., Apter, B., Baal-Zedaka, I. & Efron, U. Resolution improvement of surface plasmon-enhanced, liquid crystal spatial light modulator: simulation studies. Opt. Commun. 281, 4788–4792 (2008).
- 26. Yariv, A. & Yeh, P. Photonics: Optical Electronics in Modern Communications (Oxford Univ. Press, New York, 2006).

- Xiong, C., Pernice, W. H. & Tang, H. X. Low-loss, silicon integrated, aluminum nitride photonic circuits and their use for electro-optic signal processing. *Nano Lett.* 12, 3562–3568 (2012).
- Lin, H. H. et al. 2017. Enhanced effective second-order nonlinearities in Si-rich SiN_x thin films. In 2017 Conference on Lasers and Electro-Optics (CLEO) SM1M.6 (Optical Society of America, 2017).
- Shen, S., Liu, T. & Guo, J. Optical phase-shift detection of surface plasmon resonance. Appl. Opt. 37, 1747–1751 (1998).
- Kurihara, K. & Suzuki, K. Theoretical understanding of an absorption-based surface plasmon resonance sensor based on Kretchmann's theory. *Anal. Chem.* 74, 696–701 (2002).
- 31. Raether, H. in Surface Plasmons on Smooth and Rough Surfaces and on Gratings 91–116 (Springer, Berlin, 1988).
- Deng, S., Wang, P. & Yu, X. Phase-sensitive surface plasmon resonance sensors: recent progress and future prospects. Sensors 17, 2819 (2017).
- An, Z., Men, C., Xu, Z., Chu, P. K. & Lin, C. Electrical properties of AlN thin films prepared by ion beam enhanced deposition. *Surf. Coatings Technol.* 196, 130–134 (2005).
- Rauthan, C. M. S. & Srivastava, J. K. Electrical breakdown voltage characteristics of buried silicon nitride layers and their correlation to defects in the nitride layer. *Mater. Lett.* 9, 252–258 (1990).
- Yota, J. Effects of deposition method of PECVD silicon nitride as MIM capacitor dielectric for GaAs HBTtechnology. ECS Trans. 35, 229–240 (2011).
- McManamon, P. F. et al. A review of phased array steering for narrow-band electrooptical systems. *Proc. IEEE* 97, 1078–1096 (2009).
- Swanson, G. J. 1989. Binary Optics Technology: The Theory and Design of Multi-level Diffractive Optical Elements Report No. TR-854 (Massachusetts Institute of Technology Lincoln Laboratory, Lexington, 1989).
- 38. Broomfield, S. E., Neil, M. A. A., Paige, E. G. S. & Yang, G. G. Programmable binary phase-only optical device based on ferroelectric liquid crystal SLM. *Electron. Lett.* **28**, 26–28 (1992).
- 39. Weigel, P. O. et al. Lightwave circuits in lithium niobate through hybrid waveguides with silicon photonics. *Sci. Rep.* **6**, 22301 (2016).
- Chang, L. et al. Heterogeneous integration of lithium niobate and silicon nitride waveguides for wafer-scale photonic integrated circuits on silicon. Opt. Lett. 42, 803–806 (2017).
- Heck, M. J. Highly integrated optical phased arrays: photonic integrated circuits for optical beam shaping and beam steering. *Nanophotonics* 6, 93–107 (2017).

Acknowledgements

This work was supported by the Defense Advanced Research Projects Agency (DARPA), DARPA NLM, DARPA MOABB, the Office of Naval Research (ONR) Multidisciplinary University Research Initiative (MURI), the National Science Foundation (NSF) grants DMR-1707641, CBET-1704085, ECCS-1405234, ECCS-1644647, CCF-1640227 and ECCS-1507146, the NSF ERC CIAN, the Semiconductor Research Corporation (SRC), the NSF's NNCI San Diego Nanotechnology Infrastructure (SDNI), the Chip-Scale Photonics Testing Facility (CSPTF), Nano3, the Army Research Office (ARO) and the Cymer Corporation.

Author contributions

A.S. designed and characterized the PPPM and experimental set-ups, with input from A.E. and Y.F. Device fabrication was performed by A.S. and F.V. Design feedback for high speed characterization and performance analysis was provided by S.P. A.S., A.E.A. and Y.F. wrote the manuscript with input from S.P. and F.V. Y.F. supervised the project.

Competing interests

The authors declare no competing interests.

Additional information

Supplementary information is available for this paper at https://doi.org/10.1038/s41566-019-0360-3.

Reprints and permissions information is available at www.nature.com/reprints.

Correspondence and requests for materials should be addressed to A.S.

Publisher's note: Springer Nature remains neutral with regard to jurisdictional claims in published maps and institutional affiliations.

© The Author(s), under exclusive licence to Springer Nature Limited 2019

ARTICLES NATURE PHOTONICS

Methods

PPPM fabrication and operation. Patterning of the electrode matrix on the sapphire substrate was performed using electron-beam lithography followed by liftoff. Lithography was performed using a Raith 50 Electron Beam Writer on a 200-nm-thick spin-coated film of poly(methyl methacrylate). A 50 nm layer of Au was deposited using a Temescal BJD 1800 Ebeam Evaporator followed by liftoff. Once the electrodes were patterned, one of three different dielectrics thin films were deposited to serve as a modulation layer: a 100 nm film of AlN, a 200 nm AlN film or a 93 nm film of SRN. AlN was deposited by RF sputtering using a Denton Discovery 18. SRN was deposited using an Oxford Plasmalab 80plus PECVD with an SiH₄ flow rate of 500 s.c.c.m. For the Kretschmann configuration prism, a 25 mm × 28 mm 74° Brewster angle Si prism was used with a 48 nm Ag film deposited with a Temescal BJD 1800 Ebeam Evaporator. Optical contact was achieved by mechanically clamping the sapphire wafer hosting the electrode matrix to the Si prism, as illustrated in Fig. 1. Electrical contact from the synthesizer (Agilent MXG N5181A) was achieved via a custom probe contacting both the patterned 50-nm-thick Au contacts on the sapphire host wafer and the SPR layer during mechanical clamping of the host wafer and prism.

MZI gigahertz electrooptic modulation characterization. SPR-induced phase modulation was detected using a MZI, as shown in Fig. 2a. A fibre-coupled 1,550 nm laser (Agilent 8164B/81571A) amplified with an erbium-doped fibre amplifier (Optilab EDFA-GB-23, measured noise figure of 5.6 dB) was used as the light source. The light was focused using an adjustable focus fibre coupler to a 0.2 mm spot size and then p-polarized using a polarizing beamsplitter. The p-polarized light was then incident on a 90-10 non-polarizing beamsplitter; 90% of the p-polarized light was directed along the PPPM arm and 10% along the reference arm. Because there is approximately 10 dB of insertion loss for the 48 nm Ag-based PPPM, this 90–10 splitting is useful for achieving a coarse balance between the two arms of the interferometer. Fine balancing of the instensity of output light in the modulator arm of the MZI with respect to the reference arm was achieved by imparting a slight rotational offset to the PPPM via a rotation stage, thereby exploiting the strong angular dependence of reflectivity under SPR conditions (Supplementary Fig. 2). Light along the modulation arm was then incident on the described PPPM where a phase shift was imparted via coupling into the SPR modes supported by the modulator. A single pixel ($45 \,\mu\text{m} \times 30 \,\mu\text{m}$) of the electrode matrix was fed with a sinusoidal waveform from an electrical synthesizer (Agilent MXG N5181A) at a frequency of 1 GHz with a sourced RF power of 21 dBm (120 mW). To operate the modulator, the 48 nm Ag film on the Si prism was kept grounded while electrical contact was made to an Au contact pad on the sapphire wafer connected to an electrode of the electrode matrix via an 8-μm-wide, 50-nm-thick, ~2-mm-long patterned wire. This wire, combined with a ground plane provided by the SPR film, forms a short micro-patch transmission line. The driving field was applied across the dielectric between the electrode and the 48 nm Ag film. The light was then reflected and recombined with the reference arm at a second non-polarizing beamsplitter and then coupled back into a fibre by an adjustable-focus fibre coupler. The fibre-coupled light was then fed to an electrooptic converter (Agilent 11982A Lightwave Converter) and the

resulting waveform was measured by an oscilloscope (Agilent DSA91304A Digital Signal Analyzer).

Using precision stages, the lengths of the reference arm were adjusted to bias the output of the interferometer at a null (dark fringe) when no signal was applied from the synthesizer. Likewise, during the measurements, the incident angle on the PPPM was adjusted with a precision rotation stage to maximize the extinction ratio. The resulting electronic signal was then fed to an oscilloscope.

The capacitances of the individual $45 \, \mu m \times 30 \, \mu m$ electrodes were approximated using $C = \varepsilon_0 \varepsilon_r \frac{A}{d}$. For AlN at $d = 100 \, \text{nm}$ and $200 \, \text{nm}$, the capacitance of an individual pixel was calculated as $0.5 \, \text{pF}$ and $0.25 \, \text{pF}$, respectively. For a pixel with 93 nm SRN, the capacitance was $1.1 \, \text{pF}$. Plasmonic modulators are typically capacitance limited; assuming a driving signal resistive load of $50 \, \Omega$, the calculated RF bandwidths of the 93 nm SRN matrix were $2.9 \, \text{GHz}$ and $12.7 \, \text{GHz}$ for the $100 \, \text{nm}$ AlN matrix.

Polarization contrast imaging. A diagram of the polarization contrast imaging set-up is provided in Fig. 2b and described in further detail in Supplementary Section 2. The imaging set-up was based on reported SPR polarization contrast imaging systems¹⁷⁻²⁰. A fibre-coupled 1,550 nm laser (Agilent 81571 A) coupled to a polarization-maintaining fibre was used as the light source. The light was collimated using a Thorlabs PAF2S-5C fibre coupler to an 870 µm spot size and was then linearly polarized +45° from the p-axis using a Newport 10WLP08 polarizer. The light was then incident on the described PPPM where a spacevariant SPR-induced phase shift was imparted on the p component of the reflected light, adding a phase delay between the co-linear p and s components of the reflected light. The light passed through a $\lambda/4$ retarding plate then passed through another wire grid polarizer (Thorlabs WP25M-UB), serving as the analyser. The analyser was rotated such that the unmodulated transmitted light was located at a transmission minimum; this process of light extinction is described at length in ref. 17. The intensity contrast between the two modulation states, 'on' and 'off', is maximized at $\Theta = \psi + \frac{\pi}{2} + \sqrt{\arctan(1-e^2)^{19}}$, where ψ is the angle of the major axis of the polarization ellipse of the superposition of $\mathbf{E}_{\mathrm{p}} + \mathbf{E}_{\mathrm{s}}$ and e is the eccentricity of that polarization ellipse (Supplementary Section 2). For our experimental system, this occurred at $\Theta \approx -32.1^{\circ}$. When an electrode of the PPPM induced a refractive index shift in the dielectric modulation layer, the incident light experienced an additional phase shift on reflection. Light that was incident on the SPR thin film immediately beneath that electrode experienced an SPR-induced phase shift (moving away from the transmission minima) that is different from the SPR phase shift in unmodulated areas of the PPPM. The phase-modulated light then passed through an imaging lens doublet and was projected onto a CCD infrared camera (FLIR SC2600). This SPR polarization contrast imaging set-up is illustrated in Fig. 2b. Figure 4 shows the polarization contrast images taken by the CCD. The dark areas correspond to areas with an unmodulated SPR phase shift, which was predominantly filtered by the analyser. The bright areas correspond to areas with an electrooptically modified SPR shift.

Data availability

The data that support the plots within this paper and other findings of this study are available from the corresponding author upon reasonable request.

Nature Research, brought to you courtesy of Springer Nature Limited ("Nature Research")

Terms and Conditions

Nature Research supports a reasonable amount of sharing of content by authors, subscribers and authorised or authenticated users ("Users"), for small-scale personal, non-commercial use provided that you respect and maintain all copyright, trade and service marks and other proprietary notices. By accessing, viewing or using the nature content you agree to these terms of use ("Terms"). For these purposes, Nature Research considers academic use (by researchers and students) to be non-commercial.

These Terms are supplementary and will apply in addition to any applicable website terms and conditions, a relevant site licence or a personal subscription. These Terms will prevail over any conflict or ambiguity with regards to the terms, a site licence or a personal subscription (to the extent of the conflict or ambiguity only). By sharing, or receiving the content from a shared source, Users agree to be bound by these Terms.

We collect and use personal data to provide access to the nature content. ResearchGate may also use these personal data internally within ResearchGate and share it with Nature Research, in an anonymised way, for purposes of tracking, analysis and reporting. Nature Research will not otherwise disclose your personal data unless we have your permission as detailed in the Privacy Policy.

Users and the recipients of the nature content may not:

- 1. use the nature content for the purpose of providing other users with access to content on a regular or large scale basis or as a means to circumvent access control;
- 2. use the nature content where to do so would be considered a criminal or statutory offence in any jurisdiction, or gives rise to civil liability, or is otherwise unlawful;
- 3. falsely or misleadingly imply or suggest endorsement, approval, sponsorship, or association unless explicitly agreed to by either Nature Research or ResearchGate in writing;
- 4. use bots or other automated methods to access the nature content or redirect messages; or
- 5. override any security feature or exclusionary protocol.

These terms of use are reviewed regularly and may be amended at any time. We are not obligated to publish any information or content and may remove it or features or functionality at our sole discretion, at any time with or without notice. We may revoke this licence to you at any time and remove access to any copies of the shared content which have been saved.

Sharing of the nature content may not be done in order to create substitute for our own products or services or a systematic database of our content. Furthermore, we do not allow the creation of a product or service that creates revenue, royalties, rent or income from our content or its inclusion as part of a paid for service or for other commercial gain. Nature content cannot be used for inter-library loans and librarians may not upload nature content on a large scale into their, or any other, institutional repository.

To the fullest extent permitted by law Nature Research makes no warranties, representations or guarantees to Users, either express or implied with respect to the nature content and all parties disclaim and waive any implied warranties or warranties imposed by law, including merchantability or fitness for any particular purpose.

Please note that these rights do not automatically extend to content, data or other material published by Nature Research that we license from third parties.

If you intend to distribute our content to a wider audience on a regular basis or in any other manner not expressly permitted by these Terms please contact us at

onlineservice@springernature.com

The Nature trademark is a registered trademark of Springer Nature Limited.